Title
Flow rate dictates permeability enhancement during fluid pressure oscillations in laboratory experiments

Authors
Candela, Thibault
Brodsky, Emily E
Marone, Chris
et al.

Publication Date
2015-01-14

Peer reviewed

Flow rate dictates permeability enhancement during fluid pressure oscillations in laboratory experiments

Thibault Candela[1,2], Emily E. Brodsky[2], Chris Marone[1], Derek Elsworth[1]

1.Dept Geosciences, Penn State Univ, University Park, PA, United States.
2.Dept Earth Sciences, UC Santa Cruz, Santa Cruz, CA, United States.

Abstract

Seismic waves have been observed to increase the permeability in fractured aquifers. A detailed, predictive understanding of the process has been hampered by a lack of constraint on the primary physical controls. What aspect of the oscillatory forcing is most important in determining the magnitude of the permeability enhancement? Here we present laboratory results showing that flow rate is the primary control on permeability increases in the laboratory. We fractured Berea sandstone samples under triaxial stresses of tens of megapascals, and applied dynamic fluid-stresses via pore pressure oscillations. In each experiment, we varied either the amplitude or the frequency of the pressure changes. Amplitude and frequency each separately correlated with the resultant permeability increase. More importantly, the permeability changes correlate with the flow rate in each configuration, regardless of whether flow rate variations were driven by varying amplitude or frequency. We also track the permeability evolution during a single set of oscillations by measuring the phase lags (time delays) of successive oscillations. Interpreting the responses with a poroelastic model shows that 80% of the permeability enhancement is reached during the first oscillation and the final permeability enhancement scales exponentially with the imposed change in flow rate integrated over the rock volume. The establishment of flow rate as the primary control on permeability enhancement from seismic waves opens the door to quantitative studies of earthquake-hydrogeological coupling. The result also

suggests that reservoir permeability could be engineered by imposing dynamic stresses and changes in flow rate.

I. Introduction

Transient permeability enhancement produced by dynamic stresses is now a well-documented observation in fractured aquifers (Elkhoury et al., 2006; Xue et al., 2013; Lai et al., 2014). These studies show that shaking of the shallow crust during the passage of seismic waves generates transient permeability enhancement. A better understanding of this complex coupling between the fractured aquifer properties and the dynamic stresses is important for both fundamental and applied sciences. The fluid and pressure redistributions associated with the change in permeability may destabilize critically stressed faults (Brodsky et al., 2003; Brodsky and Prejean, 2005; van der Elst et al., 2013). Petroleum engineering could potentially employ the mechanism to design artificial dynamic shaking of fractured aquifer and enhance oil recovery (Beresnev and Johnson, 1994; Nikolaevskiy et al., 1996; Roberts et al., 2003).

One way to better characterize the process of permeability enhancement by dynamic stresses is to perform experiments on fractured rock samples (Roberts, 2005; Roberts and Abdel-Fattah, 2009; Liu and Manga, 2009; Elkhoury et al., 2011; Faoro et al., 2012; Candela et al., 2014). Recently, experiments of Elkhoury et al. (2011) and Candela et al. (2014) have successfully reproduced field observations.

The experimental technique used by Elkhoury et al. (2011) and Candela et al. (2014) consists of applying dynamic fluid-stresses via pore pressure oscillations on rock sample. These experiments have demonstrated that the magnitude of the permeability enhancement is positively correlated with the amplitude of the dynamic strain for a fixed frequency. This result is encouraging as the field observations also suggest that permeability enhancement scales with the peak ground velocity (Elkhoury et al., 2006).

Brodsky et al. (2003) and Elkhoury et al. (2011) proposed that a flow-driven process could be reasonable for transient permeability enhancement. Micromechanically, the imposed change in flow rate during the passage of seismic waves could unclog fractures or pores blocked by fines. Candela et al. (2014) confirmed the unclogging hypothesis for the laboratory experiments. However, because fine mobilization through a porous medium is a complex, multiphase process, the previous works did not establish any specific controlling variable that could potentially be used to evaluate (or even control) this effect in natural, field settings. Establishing the key parameters that govern the permeability enhancement is a necessary step in scaling the laboratory experiments to nature.

The fact that the flushing is driven by the fluid flow suggests that flow rate may be the key variable, but simply varying amplitude of the pore pressure of a single frequency is not enough to evaluate this possibility. Both sets of experiments performed by Elkhoury et al. (2011) and Candela et al. (2014) consist of imposing multiple sets of pore pressure oscillations of varying amplitudes while keeping constant the frequency and the duration of the oscillatory forcing. Here we vary frequency to probe the suspected correlation between the imposed change in flow rate and the permeability enhancement. We also use a model of porous flow within our samples to track changes in permeability and the spatio-temporal evolution of flow rate during pressure oscillations. The combination of the frequency and amplitude variations and the poromechanical model interpretations of flow will help illuminate the factors that dictate flow rate and permeability evolution.

This paper builds on the understanding that colloidal mobilization is the fundamental unclogging process in the lab and strives to build enough of a quantitative understanding of the controlling variables to set the stage for scaling the laboratory results to the field. To this end, we begin with a description of the laboratory apparatus (Section II.1) and experimental set-up (Sections II.2-3) and then present measurements of flow and deformation during the pore pressure oscillations (Section III), which demonstrate permeability enhancement (Section IV). In Section V we make the connection between flow rate, during pressure oscillations, and permeability enhancement by making use of poromechanical analysis and in particular the 1D diffusion problem during pore pressure oscillation. Finally, we discuss the extrapolation of our experimental results to the field system scale in two steps (Section VI). First, the complicating factor of coupling to the elastic, seismic waves to the pore pressure is evaluated using an additional experiment that applied solid mechanical stresses instead of fluid stresses (Section

VI.1-2). Second, we explore the application to the field conditions of our experimental prediction in term of scaling between the imposed change in flow rate and the resulting permeability enhancement (Section VI.3).

II. Experimental Method

II.1. A true triaxial pressure vessel

We performed experiments on fractured samples of Berea Sandstone using a direct shear configuration within a pressure vessel (Figure 1). A true triaxial stress state was achieved via the confining pressure and two loads applied through the piston (for details of the apparatus, see Samuelson et al., 2009 and Ikari et al., 2009). In addition to the confining pressure, a horizontal ram applies a force normal to the fracture plane, and the vertical ram of the biaxial load frame is used to apply stress to the top of the sample.

Two pore pressure intensifiers were used to control fluid pressure (or flow rate) and measure permeability (Figure 1). We measured inlet and outlet flow volumes to a resolution of 5.1 x 10^{-5} cm^3 using Linear Variable Differential Transformers (LVDTs) mounted on the pressure intensifier pistons. The effective permeability k is determined from Darcy's law (Equation 1). Flow rates were measured independently at both the inlet and outlet to verify steady state flow and permeability was determined using Darcy's Law:

$$k = \frac{\mu L}{S} \frac{Q}{\Delta Pp} \qquad (1)$$

where μ is the fluid viscosity (8.9×10^{4} Pa.s), L is the flow path i.e. the sample length (50 mm), S is the cross section of the sample perpendicular to the flow path (45 x 29 mm), and ΔPp is the differential pore pressure between the inlet and outlet (Figure 1). In the data presented below, we always verified that inlet and outlet flow rate were equal to within ≤1% before measuring permeability.

Each axis of triaxial loading is servo-controlled independently and all stresses, strains, fluid pressures and fluid volumes were measured continuously with a 24-bit analog to digital converter at 10 kHz and averaged to recording rates of 1 to 100 Hz depending on the experiment stage.

Vertical and horizontal displacements of the applied loading rams were measured with Direct-Current Displacement Transducers (DCDT) mounted on the biaxial load frame with ±0.1 μm precision (Figure 1). To determine elastic strain and any changes in the sample thickness, we used an LVDT mounted across the sample within the pressure vessel with a ±0.025 μm precision. Applied stresses were measured with strain gauge load cells, calibrated with a proving ring traceable to the National Bureau of Standards, and recorded with force resolution of ± 10 N

(~4.4 kPa on the fracture plane which has nominal dimensions of 45 mm x 50 mm). Fluid pressures were measured using transducers mounted at the pressure intensifiers accurate to ± 0.007 MPa.

II.2. Experimental procedure

Samples of Berea Sandstone were: (1) cut into L-shaped blocks measuring 68 x 45 x 50 x 29 mm, (2) presaturated with the pore fluid of deionized (DI) water, (3) jacketed in a latex membrane and (4) placed in the direct shear configuration. As discussed by Candela et al. (2014), the water chemistry is significant factor in particulate mobilization. For these experiments we selected DI as a simple aqueous chemistry that was easily reproduced.

Experiments started with application of a small normal stress across the future fracture plane, after which confining pressure was applied. Normal stress and confining pressures were then raised to the target values of 20 MPa and 9 MPa respectively. These stresses were then maintained constant in load feedback control.

The next step was to initialize fluid flow through the samples. Pore pressures (Pp) were servo-controlled independently and applied via a line source at an inlet and outlet such that flow occurred along the future fracture plane (Figure 1). The fluid inlet and outlet each consists of a narrow channel (1 mm wide 45 mm long) fed by five 1/16” (1.6 mm) dia. holes in order to homogeneously distribute the flow along the width of the sample (Figure 1). We applied first a controlled pore pressure at the outlet and flushed the system until clear fluid (without air bubbles) flowed from the inlet, which was open to the atmosphere. Then the inlet pore pressure line was connected and we applied a controlled difference (*ΔPp*) (see Table 1). Pore pressures were then maintained constant except for imposed pressure oscillations.

The next step was to fracture the sample. Shear load was applied by advancing the vertical piston in servo displacement control at 10 microns/s, which increased stress on the top of the L-shaped block until the sample fracture (Figure 1). Due to the sample geometry and loading conditions, the fracture was constrained to propagate along the long-axis of the specimen - vertically in the loading apparatus. A thin starter-notch was added at the top of the sample in order to minimize the geometrical complexity of the fracture and to acquire a planar and reproducible fracture geometry for each experiment.

II.3. Dynamic stressing via pore pressure oscillations

After the sample fractured, we imposed sinusoidal oscillations in the upstream pore pressure while holding the downstream pore pressure constant to simulate dynamic forcing following the technique of Elkhoury et al. (2011) and Candela et al. (2014) (Figure 2). For each experiment, we imposed multiple sets of pore pressure oscillations on the fractured sample and the waiting time between two sets was around 30min.

Two kinds of pore pressure oscillation experiments are presented in this paper (Figure 2). The amplitude experiments are identical to those performed by Elkhoury et al. (2011) and Candela et al. (2014) in which multiple sets of pore pressure sinusoidal oscillations of varying amplitude A are imposed. The period (T=20s) and the duration (120s) are kept constant. In this publication, only the results obtained for one representative experiment (p4092) are presented. Additional details and results of these amplitude experiments can be found in Candela et al. (2014).

The second type of experiments, called frequency experiments, consists of multiple sets of pore pressure oscillations of varying periods (T=1s-5s-20s). The normalized amplitude (A/ΔPp~0.82) and duration (120s) are kept constant. This value of normalized amplitudes corresponds to the upper range of the amplitudes explored for the amplitude experiments (see Figure 2).

III. Flow and deformation during pore pressure oscillations

Figure 3 shows the flow and mechanical response of two representative sets of pore pressure oscillations with two frequencies (T=1s and T=20s) during the same experiment (p4167).

In these experiments, we impose sinusoidal oscillations in the upstream pore pressure while holding the downstream pore pressure constant via a fast-acting servohydraulic controller. This forces an oscillatory flow to diffuse from the top to the bottom of the sample. The peak flow rate increases progressively during each set of pressure oscillations and is globally higher for the high-frequency set (Figure 3). The flow rate attenuation R and time delay τ between the upstream and the downstream become progressively more severe and higher as frequency increases.

These experiments document the enhancement of flow rate relative to the initial flow rate (Figure 3). Because the controlled differential pore pressure is identical before and after each set, flow rate enhancement can be directly related to permeability enhancement. We find that direct permeability enhancement is higher for the high-frequency set, and is followed by a progressive recovery of the permeability for both sets.

We measure transient changes in sample thickness normal to the fracture plane and find identical magnitudes for the two sets of pore pressure oscillations (Figure 3). However the poroelastic response of the sample and the observed permeability enhancement are not connected to any measureable, permanent deformation.

IV. Direct permeability enhancement and pressure oscillations

Permeability increases systematically as a function of both pore pressure oscillation amplitude and frequency (Figure 4). Following Elkhoury et al. (2011) and Candela et al. (2014), we report permeability enhancement as $(k1\text{-}k0)/k0$ where $k0$ represents the initial permeability 10s before oscillations and $k1$ the permeability 10s after oscillations. The difference in permeability ($k1$-$k0$) is linearly dependent to the initial permeability $k0$. Consequently, in order to compare experiments with different background permeability, we normalize the difference in permeability ($k1$-$k0$) by $k0$.

For the amplitude experiments, the permeability enhancement Δk is positively correlated with the amplitude of the pore pressure oscillations (Figure 4a). This exponential relationship $\Delta k \propto e^A$ has been previously observed by Elkhoury et al. (2011) and Candela et al. (2014).

For the frequency experiments, the permeability enhancement is positively correlated with the frequency of the pressure oscillations (Figure 4b). For oscillation periods ranging from 1-5s-20s, the average permeability enhancements are respectively 70%, 25% and 10%. Note that the fixed normalized amplitude of the pore pressure oscillations, $A/\Delta Pp$ for the frequency experiments corresponds to the higher magnitudes explored in the amplitude experiments, i.e., $\mathrm{A}/\Delta Pp \sim 0.82$.

These new experimental results are tricky to interpret from the raw data. In our amplitude experiments (Figure 4a), by increasing A we increase the maximum differential pore pressure and consequently the peak flow rate following Darcy's Law. Previous work showed that unclogging is the primary mechanism of permeability increases in these experiments (Candela et al., 2014). The higher peak flow rate will flush more efficiently the temporary blockages from fractures, which explains the higher permeability enhancement by unclogging. However, in the frequency experiments, we observe a higher permeability enhancement with high frequency pore pressure oscillations, even if the pore pressure amplitude and therefore the maximum differential pore pressure are identical (Figure 3 & 4). This result is potentially confusing because in a quasi-static system Darcy's Law implies that the flow rate should depend only on the pore pressure differential across a fixed length and not the rate of pressure change.

The solution to this conundrum is to consider the diffusion of the pore pressure oscillations through the interior of the sample and fracture plane. Attenuation of the forcing signal is expected at high frequencies due to diffusion in the porous medium. There is direct evidence (Figure 3) of such a diffusive process as the outlet pore pressure oscillation is attenuated and delayed relative to the inlet. Understanding this attenuation effect as a function of frequency is therefore critical to interpreting the frequency experiments and we now proceed to use a simple, analytical model to help interpret the results.

V. Diffusion solution for flow in the interior of the sample

In order to quantitatively evaluate the effect of the frequency variation on the flow field, we model the diffusion of the pore pressure oscillation (Kranz et al., 1990; Fisher, 1992; Fisher and Paterson, 1992; Zhang et al., 1994; Bernabe et al., 2006; Song and Renner, 2007). We will first review the analytical solution and then use it to: (1) examine how the permeability changes with progressive oscillations and (2) explain the observed frequency effects by taking an appropriate volumetric average of the flow field over the sample.

Kranz et al. (1990) and Fisher (1992) derive an analytical solution of the diffusion equation for 1-D flow along a finite sample excited by a pore pressure oscillation Ae^{iwt}. The problem consists on finding Pp(x,t) such that

$$\frac{\partial Pp}{\partial t} = \mathrm{v}\frac{\partial^2 Pp}{\partial x^2} \quad (0 < x < L)$$

(2)

where v is the hydraulic diffusivity with boundary conditions:

At x = 0,

$$P(0,t) = Ae^{iwt}$$

(3)

At x = L,

$$\frac{\partial Pp}{\partial t} + \lambda \frac{\partial Pp}{\partial x} = 0 \; (\lambda > 0)$$

(4)

where $\lambda = (kS)/\mu\beta V_2$, β is the fluid compressibility (4.2×10^{-10} Pa^{-1}), and V_2 is the downstream fluid reservoir (125 cm^3). As in Equation (1), μ is the fluid viscosity (8.9×10^{4} Pa.s), L is the flow path i.e. the sample length (50 mm), and S is the cross section of the sample perpendicular to the flow path (45 x 29 mm). The periodic solution as a function of distance x from the upstream (see Figure 2) and time t is

$$Pp(x,t) = \frac{A\{[iw - \lambda(1+i)N]e^{iwt + (1+i)N(x-L)} - [iw + \lambda(1+i)N]e^{iwt - (1+i)N(x-L)}\}}{[iw - \lambda(1+i)N]e^{-(1+i)NL} - [iw + \lambda(1+i)N]e^{(1+i)NL}}$$

(5)

where $w = 2\pi/T$ is the angular velocity of the pore pressure oscillation and $N = \sqrt{(w/2v)}$. From the development of Equation (5) as detailed in Kranz et al. (1990), the amplitude ratios R and phase difference $\delta = -2\pi\tau/T$ between the upstream and downstream pore pressure are

$$R^2 = \frac{4\alpha^2}{(2\alpha^2 + 1)\cosh 2\gamma + (2\alpha^2 - 1)\cos 2\gamma + 2\alpha(\sinh 2\gamma - \sin 2\gamma)}$$

(6)

$$\delta = arc \tan \left[\frac{\tanh(2\alpha \tan\gamma + 1) + \tan\gamma}{\tan\gamma - \tanh\gamma + 2\alpha} \right]$$

(7)

where the dimensionless variables α and γ are:

$$\alpha = \lambda / \sqrt{2wv} \qquad (8)$$

and

$$\gamma = wL / \sqrt{2wv} \qquad (9)$$

Given two observables R and δ, Equations (6-7) can be solved simultaneously to extract the dimensionless variables α and γ . From these solutions and Equations (8-9), permeability and the hydraulic diffusivity are obtained. In our situation, because the upstream and downstream reservoirs are servo-controlled in pressure feedback control, we measure the amplitude ratios R and time delays τ of the flow rate between the upstream and the downstream (Figure 3).

V.1. Temporal evolution of the hydraulic diffusivity, permeability, and specific storage

Figure 5 displays the temporal evolution of the flow rate amplitude ratio and time delays during one set of pore pressure oscillations with T=1s. The pair of parameters R and δ are measured for each sinusoid, and for each R-δ pair the temporal evolution of the hydraulic diffusivity and permeability are deduced. Figure 6 shows an example of this analysis for the data of experiment p4167 presented in Figure 3. The trends shown in Figure 6 apply throughout our set of experiments of pore pressure oscillations with different amplitudes and frequencies.

We find that transport properties, the hydraulic diffusivity, and permeability increase progressively during pore pressure oscillations (Figure 6). This observation is in agreement with the progressive slight increase of the peak flow rate observed during pressure oscillations (see Figure 3). In contrast, our measurements indicate that the specific storage of the samples defined as

$$S_s = \frac{k}{\mu \nu}$$

(10)

is constant for each experiment and does not evolve during the application of the dynamic stressing (Figure 6c). The unclogging of temporary blockages via particle fracture or mobilization is not expected to affect the bulk properties such as the specific storage but only increase the interconnectivity and therefore change the transport properties such as the permeability and diffusivity.

The increase of the hydraulic diffusivity and permeability follow a logarithmic function; as we increase the diffusivity and permeability it gets harder and harder to increase them (Figure 6). For unclogging, these logarithmic increases can be a consequence of the evolution of the budget of particles blocking the fracture porosity. During the first pore pressure sinusoid, most of the particles are unclogged leading to a strong change of the transport properties, but during subsequent pressure oscillations fewer and fewer particles are susceptible to unclogging, and therefore it is harder and harder to increase the diffusivity. Following this reasoning, the number of particles flushed (ΔN) and both the permeability and diffusivity enhancements (Δk, $\Delta \nu$) should scale with the number of oscillations (n): $\Delta k \propto \Delta N \propto ln(n)$.

Interestingly, the cumulative change in hydraulic diffusivity and permeability is only 15% compared to the state during the first oscillation, while the observed permeability enhancement relative to the original state is 70% (Figure 6). In other words, during the first pore pressure sinusoid, 80% of the permeability enhancement is achieved.

V.2. Flow rate controls permeability enhancement

In the context of an unclogging mechanism driven by dynamic stressing, it seems plausible that the maximum change in flow rate should be the key parameter controlling the flushing efficiency and therefore permeability enhancement. However, we only measure the flow rate at the inlet and outlet of the sample; whereas unclogging and permeability enhancement occurs in the interior, and we measure the average permeability change for the fracture and bulk sample. Therefore, we need to consider the spatial variation of the flow rate in establishing a connection between flow rate and permeability changes.

V.2.a. Measured and modeled flow rates at the sample boundaries

Assuming that a continuum approach applies to the sample, that is, Darcy's law is applicable to spatial scales (much) smaller than the sample size, the periodic solution of the pore pressure diffusion (Equation 5) can be used to track the spatio-temporal evolution of the flow rate through the sample as

$$Q(x,t) = -\frac{kS}{\mu}\frac{\partial Pp(x,t)}{\partial x}. \qquad (11)$$

Figure 7 presents the spatio-temporal evolution of the flow rate through the sample for the data of Figure 3. These are oscillations sets with the same amplitude but two different frequencies (T=1s and T=20s).

We have already established that most of the change in transport properties that are enhancements in hydraulic diffusivity and permeability happen at the onset of the application of the dynamic stressing (Figure 6). For each set of oscillations, the first measured peak flow rate of the first sinusoid is already associated with a value of permeability close to the final value *k1*. Because we are interested in the flow before any change in transport properties, in Figure 7 we use for *k* and ν the initial values before each set of pore pressure oscillations. For *k*, we use the measured initial permeabilty *k0*. For ν, we can use our measurements of the amplitude ratios *R* and time delays δ, in order to estimate first the specific storage of each rock sample as defined by Equation (10). Then, with this value of specific storage and the measured *k0* we define the initial hydraulic diffusivity used to produce the result in Figure 7. Table 1 provides all values used to compute the spatio-temporal evolution of the flow rate through the samples.

Figure 7 and 8 reveal the attenuation-effect as a function of the frequency of pressure oscillations. At high frequency, pressure oscillations are more severely attenuated, and consequently the local peak flow rate at the top of the sample is relatively higher. In the meantime, the higher attenuation of the pore pressure oscillation at high frequency results in a relatively lower local flow rate at the bottom of the sample.

Figure 8 can be directly compared with Figure 3. The measured (Figure 3) and modeled (Figure 8) flow rates are qualitatively similar; in both cases relatively higher peak flow rates and a more severe attenuation is observed at high frequency. However, because the measured flow rates in Figure 3 are already associated with the final permeability *k1*, relatively higher absolute magnitudes in the peak flow rates are measured in Figure 3 compared to those estimated by the model in Figure 8. This difference is accentuated at high frequency due to the relatively larger permeability enhancements.

The model provides the flow rate at the upstream and downstream before the onset of permeability enhancement. In order to evaluate if the model prediction is in agreement with our experimental observations, we need to subtract from our measurements of the maximum upstream and downstream peak flow rates *Qmax*, the increase in flow rate due to the permeability enhancements, i.e.,

$$Qmax_{corrected} = Qmax - \left[\frac{(k1 - k0)(A + \Delta Pp)}{\left({}^{\mu L}/_{S}\right)}\right]$$

(12)

Figure 9 shows the maximum change in flow rate deduced from our measurements and those predicted. Figure 9 demonstrates that the analytical solution of the 1D diffusion problem is clearly in agreement with our measurements. For example, the maximum change in flow rate deduced from the corrected peak flow rate $Qmax_{corrected}$, are now roughly the same as the predicted maximum change in flow rate. Table 1 provides all values used for the model including initial specific storage, hydraulic diffusivity, and permeabilty. Note here that because the maximum change in flow rate is linearly dependent on the initial flow rate $Q0$ (see inset Figure 9), the maximum change in flow rate is normalized by $Q0$.

V.2.b. Average flow rate inside the sample

We can now compare the peak flow rate within the fracture with the permeability changes. Our measurements clearly reveal the positive correlation between the permeability enhancement and the average between the maximum change in flow rate at the upstream and downstream (Figure 9). We can make this empirical relationship more precise using the diffusive model. The volumetric average peak flow rate from the inlet to a depth L inside the rock sample is

$$Qvol = \sqrt{\frac{1}{L}\int_0^L (Qmax^2)dx}$$

(13)

Figure 10 presents the change in the volumetric average amplitude of the flow rate as $(Qvol - Qvol_0)/Qvol_0$, when $Qvol$ is the magnitude reached during the application of the dynamic stressing and $Qvol_0$ is the initial value. Figure 10 demonstrates the positive correlation between the change in flow rate integrated over the length of the sample and the permeability enhancement. The fact that the 1D diffusion model fits our flow rate measurements at the top and bottom of the sample leads us to believe that the same correlation holds between the change in flow rate integrated over the length of the sample and the permeability enhancement. In the experiments, the combined amplitude and frequency variation control the activated volume of the rock-sample and therefore the final permeability enhancement averaged over the volume.

Our analysis indicates an exponential relationship between permeability enhancements and the volumetric change in flow rate. During unclogging, the flow is removing fine particles in the fracture. We start by assuming the simplest possible relationship between the number of particles flushed (ΔN) and the flow rate change (ΔQ), i.e., a linear relationship:

$$\Delta N \propto \Delta Q \qquad (14)$$

According to Darcy's law and for a fixed path length:

$$\Delta Q \propto k0\ A \qquad (15)$$

where A is the amplitude of the imposed pore pressure oscillation and $k0$ is the initial permeability before any changes. At the end of the oscillatory forcing, we assume that the cross-sectional area of the fracture cleaned is proportional to the number of particles flushed, i.e.,

$$\Delta k \propto \Delta N \,. \qquad (16)$$

Finally, combining Equations (14-16) and integrating results in

$$ln(k) \propto A \qquad (17)$$

As revealed by our experimental results, the change in permeability is proportional to the initial permeability $\Delta k \propto k$ (inset Figure 4), implying that:

$$ln(\Delta k) \propto A \qquad (18)$$

Equation (18) is in agreement with our observation (Figure 4) and those of Elkhoury et al. (2011) and Candela et al. (2014). Finally, we note that for any change in permeability, $\Delta Q \propto A$ (Equation 15) and therefore

$$\Delta k \propto e^{\Delta Q} \qquad (19)$$

as observed in our experiments (Figure 10). The consistency means that our interpretation in term of flow-driven mechanism for permeability enhancement is reasonable. The change in flow rate integrated over the rock volume is the key parameter controlling the flushing of blockages and therefore the permeability enhancement.

VI. Extrapolation to the field scale

We address two questions related to connecting our laboratory measurements to field observations: (1) is our experimental setup appropriate for evaluating the connections between dynamic stressing and fluid flow in nature? (2) can we extrapolate our measurements to the field scale?

VI.1. Generating oscillatory flows from seismic waves

In a fractured aquifer, during the propagation of a seismic wave, the dilatational strain directly generates a hydraulic head oscillation with the local amplitude dependent on the local stiffness. Since the amplitude of the head oscillations is different in stiff, intact rocks and damaged fault zones, a flow between the units is generated locally. This flow is what we artificially reproduce in our experiments. By imposing sinusoidal oscillations in the upstream pore pressure while holding the downstream pore pressure constant, we force an oscillatory flow from the top to the bottom of the sample. The pressure oscillation technique, applied on fractured rock samples, is therefore well adapted to reproduce the passage of seismic waves through a fractured aquifer.

An alternative approach is to mimic the forcing of the seismic waves on the solid rock and then allow the pore pressure to vary as a consequence inside the sample. This approach has been taken by other experimenters who either used long-period solid mechanical forcing (Liu and Manga, 2009) or acoustic vibrations (Roberts, 2005; Roberts and Abdel-Fattah, 2009. Notably, Liu and Manga (2009) found permeability *decreases* when applying solid mechanical stresses.

In order to evaluate the differences between the solid and fluid forcing, we performed experiments in which stress oscillations were applied to the solid block rather than via a fluid pressure. Figure 11 shows results from a representative experiment. After fracturing the sample following the same preliminary procedure as for the pore pressure oscillations technique, we oscillated the stress normal to the fracture while the differential pore pressure ΔPp, the shear stress, and the confining pressure were maintained constant. Controlled normal-stress oscillations are achieved by adjusting the servo command signal for the horizontal loading ram in load feedback mode. We applied multiple sets of normal stress sinusoidal oscillations of varying amplitude while keeping constant the period (20s) and the duration (120s), and spaced in time of around 30min.

Figure 11 shows that normal-stress oscillations cause transient compaction-dilation of the rock sample as measured with the internal LVDT mounted across the fracture (Figure 1). The stress oscillations cause transient changes in fluid flow superimposed on the background initial flow (Figure 11). Squeezing fluids in and out of the fracture plane, during the normal-stress oscillation, produces the observed oscillatory flow. At the end of the stress oscillations, the flow rate (identical at the upstream and downstream boundary) is lower compared to the initial value before the oscillatory forcing.

Because ΔPp is maintained constant during imposed normal stress oscillations, the measured reduction in flow rate can be directly translated to permeability. In fact, following the application of the dynamic stress, we observe a net decrease of the sample thickness (Figure 11). The simplest interpretation is to directly relate the measured sample compaction Δu_n in term of closing of the fracture aperture. This way, the decrease in permeability is directly related to the closing of the fracture aperture. This interpretation is demonstrated in Figure 12 which shows that both the measured sample compaction Δu_n and permeability reduction increase with the amplitude of the normal-stress oscillations.

Following the most commonly used equation for fluid flow through fractures frequently called the cubic law (e.g. Snow, 1969; Witherspoon et al., 1980; Silliman, 1989; Ouyang and Elsworth, 1993), we can link *k0* and *k1* with the fracture aperture via the parallel plate approximation

$$k_0 = \frac{b_0^3}{12W} \quad (20)$$

and

$$k_1 = \frac{(b_0+\Delta b)^3}{12W} \qquad (21)$$

where b_0 is the initial aperture of the fracture, Δb is the closing of the fracture aperture and W is the width of the sample. Then combining (20) and (21), we can estimate the predicted magnitude of the permeability decrease for the observed aperture closure Δb as:

$$\left|\frac{k_1-k_0}{k_0}\right| = \frac{(\sqrt[3]{12k_0W}+\Delta b)^3}{12k_0W} - 1 \qquad (22).$$

Interestingly, the magnitude of the permeability decrease predicted by the cubic law model (Equation 22) is significantly larger than the observed permeability decrease (Figure 12c). One explanation for this discrepancy is that the permeability decrease associated with the aperture closing is mitigated by a permeability increase due to unclogging. The same unclogging mechanism as observed in the earlier experiments could cancel much of the fracture closure and result in a more modest net permeability decrease than expected from the deformation data.

A second possibility, is that the actual change in aperture within the sample is significantly less than the observed permanent compaction of the sample of $\Delta u_n \sim 20\mu m$, apparent in Figure 12c. This could result if either (1) the compactive deformation of the sample is distributed throughout the sample rather than merely concentrated on the mechanically-soft fracture (implicitly assumed in Equation (22)), or (2) that the active flow conduit is a circular cross-section pipe that is significantly more resistant to deformation than the mechanically-soft parallel plate fracture assumed in Equation (22).

(1) In the first instance, if the compactive deformation is partitioned on the fracture in proportion to the stiffnesses of the intact rock (E_i) and the fractured composite (E_m) (Ouyang and Elsworth, 1993) then the change in aperture is given as

$$\Delta b = [W(1-R_m)+b_0]\Delta u_n / W \quad (23)$$

where $R_m = E_m / E_i$. For the measured magnitude of $R_m = 0.4$ and with $\Delta u_n = 20\mu m$ this results in an expected change in aperture of $\Delta b \sim 0.6\Delta u_n = 12\mu m$. Although smaller than the measured permanent compaction of the sample, this magnitude remains still too large to explain the observed very small reduction in permeability.

(2) Alternately, where the active flow is considered confined to a single tubular flow conduit then the volumetric flow rate Q scales with pipe diameter, D, as $Q_0 \propto D_0{}^4$ or with the modified diameter as $Q_1 \propto (D+\Delta D)^4$. The change in diameter of a circular section tube embedded within an elastic medium scales as $\Delta D \sim D_0 \Delta\epsilon$ where $\Delta\epsilon$ is the isotropic strain applied to the elastic medium. This allows the change in permeability anticipated from a single compressible flow tube to be approximated as

$$\left|\frac{k_1 - k_0}{k_0}\right| = \frac{Q_1 - Q_0}{Q_0} \propto (1+\frac{\Delta u_n}{W})^4 - 1 \quad (24)$$

where the permanent strain retained within the sample is identified as $\Delta\epsilon = \Delta u_n / W$ (Figure 12; $2\mu m < \Delta u_n < 35\mu m$). This enables the observed permanent post-oscillation change in permeability to be compared with that predicted from the presumed representation of the system as a geometrically-soft parallel-sided fracture (Equation (22)) versus a geometrically-stiff pipe (Equation (24)) in Figure 12c. Apparent from this comparison is that these two end-member behaviors bracket the true response (Figure 12c) and suggesting that the true flow conduit is best represented as an elliptical section pipe with major-axis ratio larger than 1:1.

Our experiments reveal that solid mechanical stresses do not reproduce permeability enhancements as observed in the field. One key point here is that we were able to generate spontaneously an oscillatory flow (Figure 11) in contrast to the artificially-generated oscillations in flow rate with the pore pressure oscillations technique (Figure 3). At this point, we cannot exclude that using a different experimental setup allowing stronger contrast of stiffness between the fracture and the bulk of the sample, we could drive stronger oscillatory flows and possibly permeability enhancements. However, it is important to note that during the solid-stresses experiment the imposed dynamic strains were one order of magnitude larger (~ 10^{-5}) compared to those imposed during the dynamic fluid-stresses experiments (~10^{-6}).

VI.2. Application to field conditions

One of our main goals was to identify the variable controlling the permeability enhancement during the passage of seismic waves through a fractured aquifer (Elkhoury et al., 2006; Xue et al., 2013; Lai et al., 2014). Previous experiments of Elkhoury et al. (2011) and Candela et al. (2014) have suggested that during the passage of a seismic wave, at a given frequency the amplitude of the pore pressure oscillations directly induced by the dilatational strain, could be the variable controlling the measured permeability enhancement. Here our experimental results reveal that once a range of frequencies is considered, the flow velocity is the preferred discriminant. As might be expected from an unclogging mechanism, higher volumetric changes in flow velocity induce higher permeability enhancements.

Our work suggests that a better knowledge of the change in flow rate through the volume of rock subject to dynamic stressing is key to predicting subsequent permeability enhancement. One can ask now if we can use our experimental correlation between the volumetric change in flow rate and the permeability enhancement (Figure 10) for field predictions. In order to answer this question, it remains to estimate the change in flow velocity around boreholes where permeability enhancements have been observed. This can be estimated by considering the oscillation of the water level $\frac{dz}{dt}$ inside the borehole during the passage of seismic waves (Brodsky et al., 2003). The volume of water $\frac{dV}{dt}$ flowing in and out the cylindrical boundary of the borehole and produced by the passage of the seismic wave can be link to $\frac{dz}{dt}$ as:

$$\frac{dV}{dt} = \frac{dz}{dt} S_c = u S_A \qquad (25)$$

where u is the average flow velocity at the boundary of the borehole driven by the seismic waves where S_c and S_A are the cross-section ($S_c = \pi r^2$) and the cylindrical surface area ($S_A = 2\pi rh$) of the borehole. Note that the driven flow rate u is superposed on a background flow rate as in the experiments. Rearranging Equation (25) we can estimate the change in average flow velocity at the boundary of the borehole as a function of the oscillation of the water level as

$$u = \frac{dz}{dt} \frac{r}{2h} \qquad (26)$$

The water level oscillations observed in boreholes and produced by the passage of teleseismic surface waves are characterized by an average amplitude and period of respectively 0.1m and 20s (see Brodsky et al., 2003); as a consequence $\frac{dz}{dt} = 0.02\ m/s$. The open section h of the borehole is of 100m and its radius is 0.1m, therefore u = $1x10^{-5}$ m/s. In our experiments, the driven volumetric flow rate is around $6x10^{-8}$ m^3/s which results in an average flow velocity of $4.5x10^{-5}$ m/s, which is very close to our estimation for the change in flow rate around a borehole and due to the passage of a seismic wave.

This analysis suggests that the experiments are exploring the relevant flow regime and that the physical processes explored in the lab are likely relevant to the field (Elkhoury et al., 2006; Xue et al., 2013; Lai et al., 2014). Manipulating the flow rate in depth could be the key to controling the permeability. In future experiments on actively engineering permeability, in situ flow velocities of ~ 10^{-5} m/s should be explored to evaluate permeability enhancement.

VII. Conclusion

Our experiments have previously demonstrated that a flow-driven mechanism of unclogging of temporary blockages from fracture is the most viable candidate to explain transient permeability enhancements during the passage of seismic waves. Here we showed that the combined characteristics of the seismic wave (amplitude and frequency) and the poroelastic properties of the porous media will control the magnitude of the change in flow rate which in turn results in permeability enhancement. In the laboratory, frequency variations result in variations of the affected volume of the sample as well as the local flow rate. Measuring the flow rate in the field could be the key to predict and control the permeability enhancement of fractured aquifer or reservoir.

References:

Beresnev, I.A., and P.A. Johnson, 1994, Elastic-wave stimulation of oil production: A review of methods and results. *Geophysics*, 59, 1000–1017, doi:10.1190/1.1443645.

Bernabe, Y., Mok, U. & Evans, B., 2006. A note on the oscillating flow method for measuring rock permeability, Int. J. Rock Mech. Min. Sci and Geomech. Abstr., 43, 311–316.

Brodsky, E.E., Roeloffs, E., Woodcock, D., Gall, I., Manga, M., 2003, A mechanism for sustained groundwater pressure changes induced by distant earthquakes. *J. Geophys. Res.*, 108(B8), 2390, doi:10.1029/2002JB002321.

Brodsky, E. E., and S. G. Prejean, 2005, Newconstraints on mechanisms of remotely triggered seismicity at Long Valley Caldera. *J. Geophys. Res.*, 110, B04302, doi:10.1029/2004JB003211.

Candela, T., E. E. Brodsky, C. J. Marone and D. Elsworth, 2014. Laboratory evidence for particle mobilization as a mechanism for permeability enhancement via dynamic stressing, *Earth and Planetary Science Letters*, DOI: 10.1016/j.epsl.2014.02.025.

Elkhoury, J. E., Brodsky, E.E., Agnew, D.C., 2006, Seismic waves increase permeability. *Nature*, 441, 1135–1138, doi:10.1038/nature04798.

Elkhoury, J. E., Niemeijer, A., Brodsky, E.E., Marone, C., 2011, Laboratory observations of permeability enhancement by fluid pressure oscillation of in-situ fractured rock. *J. Geophys. Res.*, 116, B02311, doi:10.1029/2010JB007759.

Faoro, I., Elsworth, D., Marone, C., 2012, Permeability evolution during dynamic stressing of dual permeability media. *J. Geophys. Res.*, 117, B01310, doi:10.1029/2011JB008635.

Fischer, G.J., 1992. The determination of permeability and storage capacity: Pore pressure oscillation method, in Fault Mechanics and Transport Properties of Rocks. eds B. Evans & T.-F. Wong, pp. 187–211, Academic Press, San Diego.

Fischer, G.J. & Paterson, M.S., 1992. Measurement of permeability and storage capacity in rocks during deformation at high temperature and pressure, in Fault Mechanics and Transport Properties of Rocks. eds B. Evans & T.-f. Wong, pp. 213 252, Academic Press, San Diego.

Ikari, M., Saffer, D.M., Marone, C., 2009, Frictional and hydrologic properties of clay-rich fault gouge. *J. Geophys. Res.,* 114, B05409, doi:10.1029/2008JB006089.

Kranz, R.L., Saltzman, J.S. & Blacic, J.D., 1990. Hydraulic diffusivity measurements on laboratory rock samples using an oscillating pore pressure method, Int. J. Rock

Mech. Min. Sci. Geomech. Abstr., 27, 345–352.

Lai G., H. Ge, L. Xue, E. E. Brodsky, F. Huang and W. Wang, 2014. Tidal response variation and recovery following the Wenchuan Earthquake from water level data of multiple wells in the nearfield, *Tectonophysics*, in press.

Liu, W., and M. Manga, 2009, Changes in permeability caused by dynamic stresses in fractured sandstone. *Geophys. Res. Lett.*, 36, L20307, doi:10.1029/2009GL039852.

Nikolaevskiy, V.N., Lopukhov, G.P., Liao, Y., Economides, M.J., 1996, Residual oil reservoir recovery with seismic vibrations. *SPE Prod. Facil.*, 11, 89–94, doi:10.2118/29155-PA.

Ouyang, Z., and D. Elsworth, 1993, Evaluation of groundwater flow into mined panels. *Int. J. Mech. Min. Sci. Geomech. Abstr.*, 30(2), 71–79, doi:10.1016/0148-9062(93)90701-E.

Roberts, P.M., Esipov, I.B., Majer, E.L., 2003, Elastic wave stimulation of oil reservoirs: Promising EOR technology? *Leading Edge*, 22, 448–453, doi:10.1190/1.1579578.

Roberts, P.M., 2005, Laboratory observations of altered porous fluid flow behavior in Berea sandstone induced by low-frequency dynamic stress stimulation. *Acoust. Phys.*, 51, 140–148, doi:10.1134/1.2133962.

Roberts, P.M., and A.I. Abdel-Fattah, 2009, Seismic stress stimulation mobilizes colloids trapped in a porous rock. *Earth Planet. Sci. Lett.,* 284, 538–543, doi:10.1016/j.epsl.2009.05.017.

Samuelson, J., Elsworth, D., Marone, C., 2009, Shear-induced dilatancy of fluid saturated faults: Experiment and theory. *J. Geophys. Res.*, 114, B12404, doi:10.1029/2008JB006273.

Silliman, S.E., 1989, An interpretation of the difference between aperture estimates derived from hydraulic and tracer tests in a single fracture. *Water Resour. Res.*, 25(10), 2275– 2283.

Snow, D.T., 1969, Anisotropic permeability of fractured media. *Water Resources Research*, vol. 5, no 6, 1273-1289.

Song, I. and Renner, J., 2007. Analysis of oscillatory fluid flow through rock samples, Geophys. J. Int., 164, 685–696.

van der Elst N.J., Savage H.M., Keranen K.M., Abers G.A., 2013, Enhanced remote earthquake triggering at fluid-injection sites in the midwestern United States. *Science* 341 : 164–167. DOI: 10.1126/science.1238948.

Witherspoon, P.A., Wang, J.S.Y., Iwai, K., Gale, J.E., 1980, Validity of cubic law for fluid flow in a deformable rock fracture. *Water Resour. Res.,* 16(6), 1016–1024.

Xue, L., et al., 2013, Continuous permeability measurements record healing inside the Wenchuan earthquake fault zone. *Science*, 340 : 1555–1559. DOI: 10.1126/science.1237237.

Zhang, S., Paterson, M.S. & Cox, S.F., 1994. Porosity and permeability evolution during hot isostatic pressing of calcite aggregates, J. Geophys. Res., 99, 15,741 15,760.

Figure captions:

Figure 1:

Biaxial apparatus and experiment configuration. (a) Schematic of the biaxial apparatus showing horizontal and vertical pistons which provide normal and shear stresses on the fracture plane, and pressure vessel. Displacements and stresses of the two pistons are measured with Direct-Current Displacement Transducers (DCDTs) and strain gauge load cells. (b) L-shape sample of Berea Sandstone, showing the fracture plane (red dotted line) that we use to compute the shear stress (c) Photo of the single direct shear configuration with the two sample holders at both sides of the L-shape sample. As a consequence of the geometry of the configuration, the fracture plane forms vertically (red dotted line) (d) Photo of pressure vessel with front door removed showing the sample (within jacket), internal fluid piping, and loading configuration. Fluid lines are connected to servo-controlled intensifiers. Linear Variable Differential Transformers (LVDTs) mounted on the intensifier pistons are used to determine flow volumes. An LVDT mounted inside the pressure vessel provides precise measurement of changes in sample thickness during the experiment. (e) Enlargement of one of the sample holders (right side of Figure 1c). Fluid ports and internal conduits in the holders provide fluid flow through the rock sample. (f) Fracture plane after the experiments. The black dotted contour highlights the white gouge particles, which are preferentially located downstream revealing their migration.

Figure 2:

Fluid flow geometry and characteristics of the dynamical stresses. (a) Schematic of the geometry of the fluid flow relatively to the L-shape sample. Pore pressure oscillations are applied at the inlet while holding constant the outlet pore pressure. The area perpendicular to the flow direction, which is used in Darcy's law, is indicated. Note also the distance x from the upstream used for the 1-D diffusion problem in Section V. (b) The amplitude experiments consists of imposing multiple sets of pore pressure sinusoidal oscillations of varying amplitude keeping constant the period (T=20s). (c) The frequency experiments consists of imposing multiple sets of pore pressure sinusoidal oscillations of varying period (T=1-5-20s) keeping constant the amplitude. Note that the constant amplitude of the frequency experiments corresponds to the highest amplitude explored in the amplitude experiments. For both types of experiments the time duration of the pore pressure oscillations is keeping constant (120s).

Figure 3:

Flow and mechanical response during two sets of pore pressure oscillations of identical amplitude but different periods. (a) Flow rate oscillations (up) and transient changes in sample thickness (down) during the two sets of pore pressure oscillations. (b) Zoom on a part of (a) showing details of the flow rate oscillations (up) and transient changes in sample thickness (down).

Figure 4:

Permeability enhancements at the end of the pore pressure oscillations. (a) For the amplitude experiments, the magnitude of the permeability enhancement is positively correlated with the amplitude of the pore pressure oscillation. (b) For the frequency experiments, the magnitude of the permeability enhancement is positively correlated with the frequency of the pore pressure oscillation. The inset indicates the linear relationship between the difference of permeability (k1-k0) and the initial permeability k0.

Figure 5:

Evolution of the flow rate amplitude ratio (a) and time delay (b) during the oscillatory forcing.

Figure 6:

Evolution of the hydraulic diffusivity (a), permeability (b) and specific storage (c) during the oscillatory forcing. For each property, the evolution of the relative magnitude (main graph) and absolute magnitude (inset) are presented.

Figure 7:

Estimation of the frequency effect on the spatio-temporal evolution of the pore pressure (a and b) and flow rate (c and d) along the length of the rock sample during the oscillatory forcing. The left side of the figure corresponds to a pore pressure oscillation with a period of 1s (a and c) and the right side to a pore pressure oscillation with a period of 20s (b and d). For each graph, the x-axis represents the sample length with 0m corresponding to the top of the sample or the upstream limit, and 0.05m the bottom of the sample or the downstream limit. See the Figure 2 to evaluate the geometry of the sample relatively to these graphs.

Figure 8:

Estimation of the frequency effect on the pore pressure (a) and flow rate (b) at the upstream and downstream limits. These graphs are directly deduced from Figure 7 in order to be compared with the experimental measurements of Figure 3.

Figure 9:

Comparison of the changes in flow rates measured in our experiments (a and c) and those deduced from the 1D diffusion model (b and d). The upstream and downstream flow rates are presented on the top-graphs (a and b). The average values between the upstream and the downstream flow rates are presented on the bottom-graphs (c and d). A visual inspection of the graphs reveals the strong correlation between the experimental measurements and the model. The inset in (c) indicates the linear relationship between the change in flow rate and the initial background flow rate.

Figure 10:

Exponential relationship between the estimated volumetric change in flow rate and the measured permeability enhancement.

Figure 11:

Flow and deformation during dynamic solid-stress oscillation. (a) Controlled normal-stress oscillations applied via the horizontal piston while maintaining constant the differential Pp. (b) Example of imposed normal-stress sinusoidal oscillation with an amplitude of 4MPa. (c) During the normal-stress oscillation we observe the transient deformation of the rock sample perpendicular to the fracture plane. At the end of the application of the dynamic stress, note the strong sample compaction normal to the fracture plane. (d) The transient compaction-dilation of the rock sample during the application of the dynamic stress induces an oscillation of the upstream and downstream flow rates. Note here the net decrease of the flow rates at the end of the application of the dynamic stress.

Figure 12:

Fracture compaction and permeability decrease at the end of the dynamic solid-stresses oscillations. (a and b) The magnitudes of the permeability decrease and sample compaction are positively correlated with the amplitude of the normal-stress oscillations. Note that for two successive sets of identical normal-stress amplitudes (t1-t2 or t3-t4), the magnitude of the sample compaction and therefore the permeability decrease are relatively higher for the first set (t1 or t3). (c) Comparison between the measured permeability decreases (data) and those predicted by the parallel-sided model and the flow-pipe model.

Table 1. Parameters of the experiments

Type of experiment	Fluid-stresses				Solid-stresses
	amplitude experiments	frequency experiments			
Exp. #	p4092	p4146	p4167	p4197	p4145
Eff. normal stress (MPa)	20	20	20	21	20.5
Failure shear stress (MPa)	37	31	27	40	34
Residual shear stress (MPa)	20	22	19	23	20
Shear offset (mm)	1	1.1	2	0.5	0.5
Confining Pressure (MPa)	9	9	9	9	9
Inlet pore pressure (MPa)	3.1	3.02	3.02	3.02	3.03
Outlet pore pressure (MPa)	2.5	2.85	2.85	2.85	2.81
Pore pressure amplitude (MPa)	0.18-0.5	0.14	0.14	0.14	
Period (s)	20	1;5;20	1;5;20	1;5;20	20
Normal-stress amplitude (MPa)					0.8-4.2
k0 (m^2)	1.6×10^{-15}	3.2×10^{-15}	1.2×10^{-14}	6.1×10^{-15}	4.3×10^{-15}
ν0 (m^2/s)	2.03×10^{-4}	4×10^{-4}	2.6×10^{-3}	1.4×10^{-3}	
Ss (Pa^{-1})	0.9×10^{-8}	0.9×10^{-8}	0.5×10^{-8}	0.5×10^{-8}	

Figure 1:

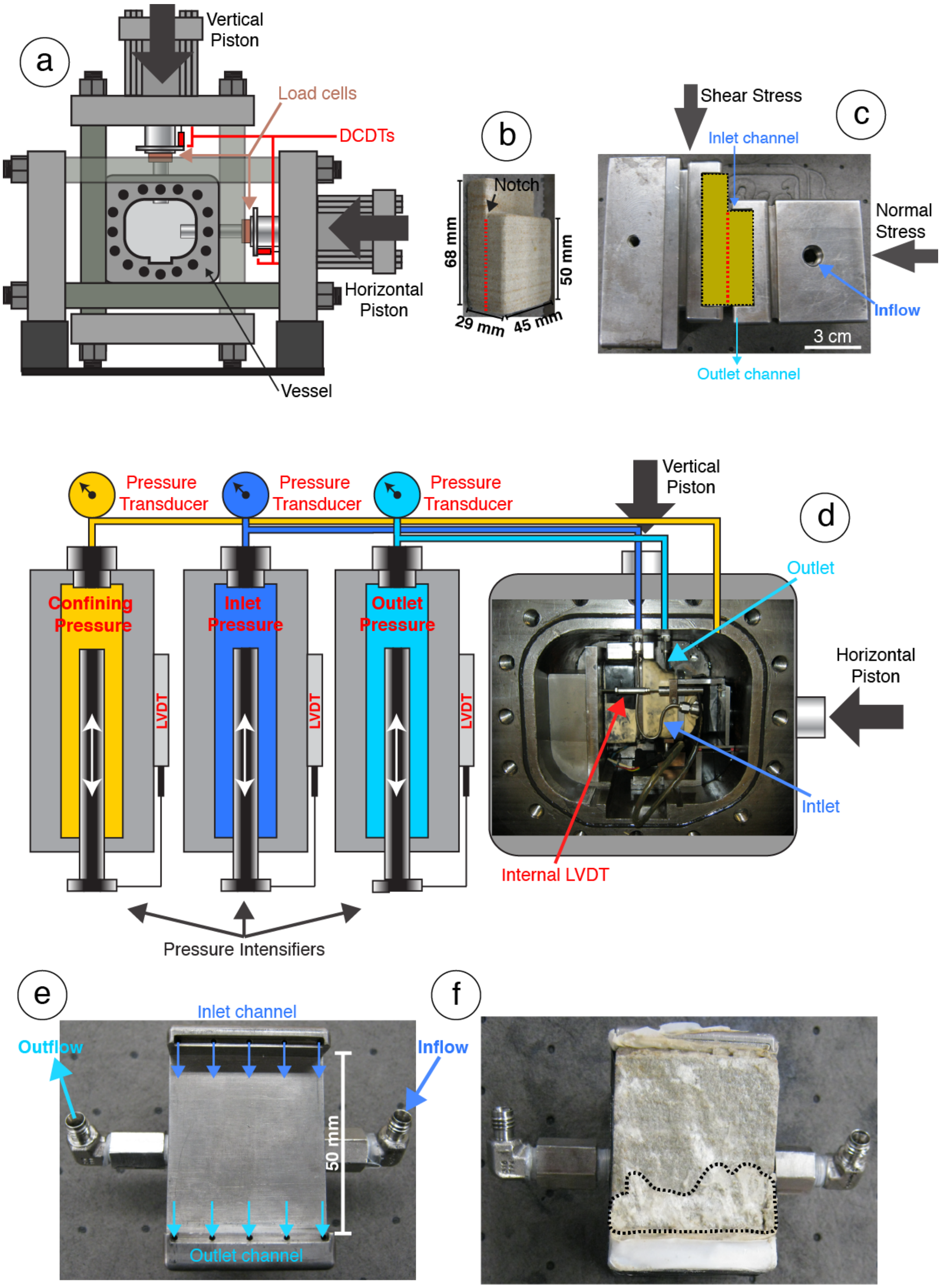
a
Vertical Piston
Load cells
DCDTs
Horizontal Piston
Vessel
b
Notch
68 mm
50 mm
29 mm
45 mm
c
Shear Stress
Inlet channel
Normal Stress
Inflow
3 cm
Outlet channel
Pressure Transducer
Pressure Transducer
Pressure Transducer
Vertical Piston
d
Outlet
Confining Pressure
Inlet Pressure
Outlet Pressure
LVDT
LVDT
LVDT
Horizontal Piston
Intlet
Internal LVDT
Pressure Intensifiers
e
Inlet channel
Outflow
Inflow
50 mm
Outlet channel
f

Figure 2:

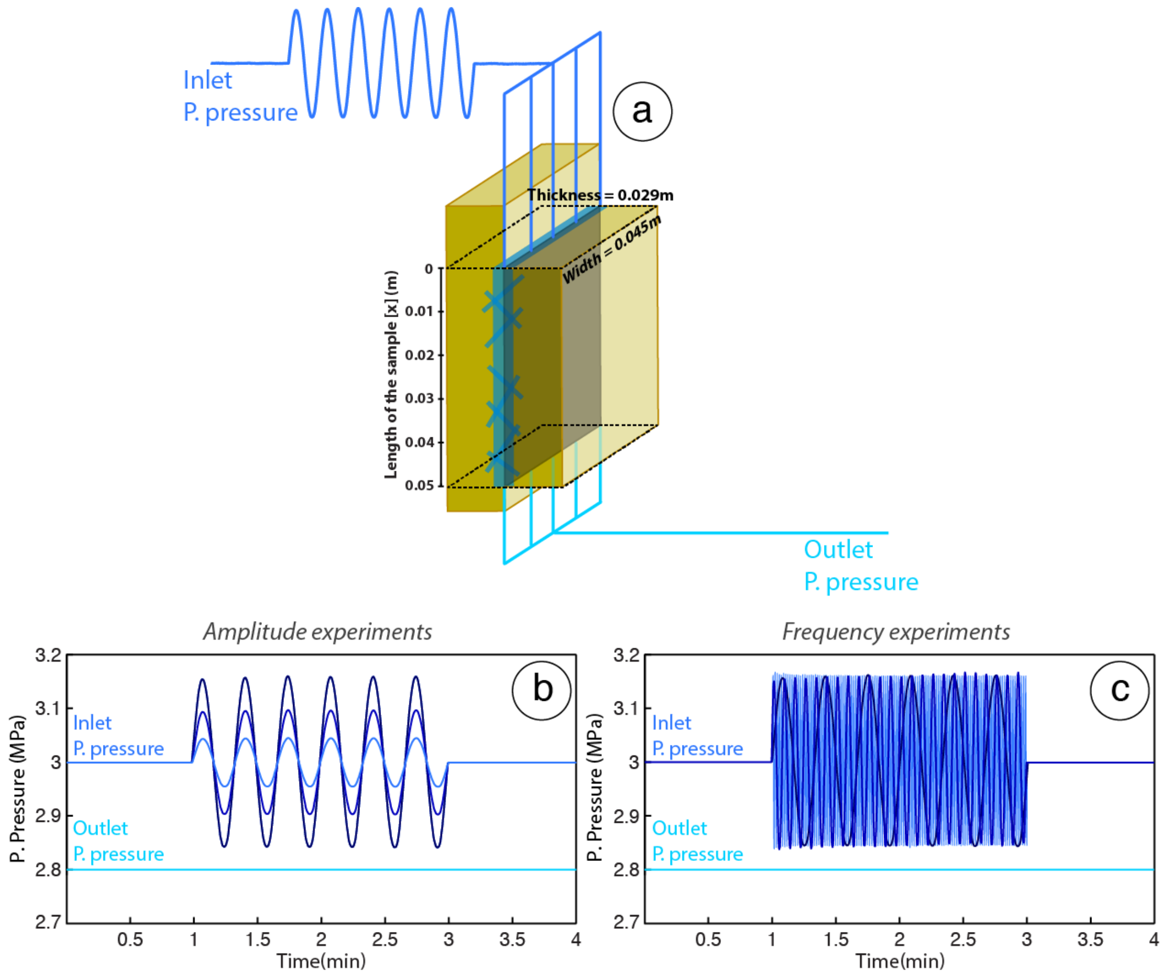

Inlet
P. pressure
a
Thickness = 0.029m
Width = 0.045m
Length of the sample [x] (m)
0
0.01
0.02
0.03
0.04
0.05
Outlet
P. pressure
Amplitude experiments
Frequency experiments
b
c
P. Pressure (MPa)
3.2
3.1
3
2.9
2.8
2.7
Inlet
P. pressure
Outlet
P. pressure
0.5
1
1.5
2
2.5
3
3.5
4
Time(min)

Figure 3:

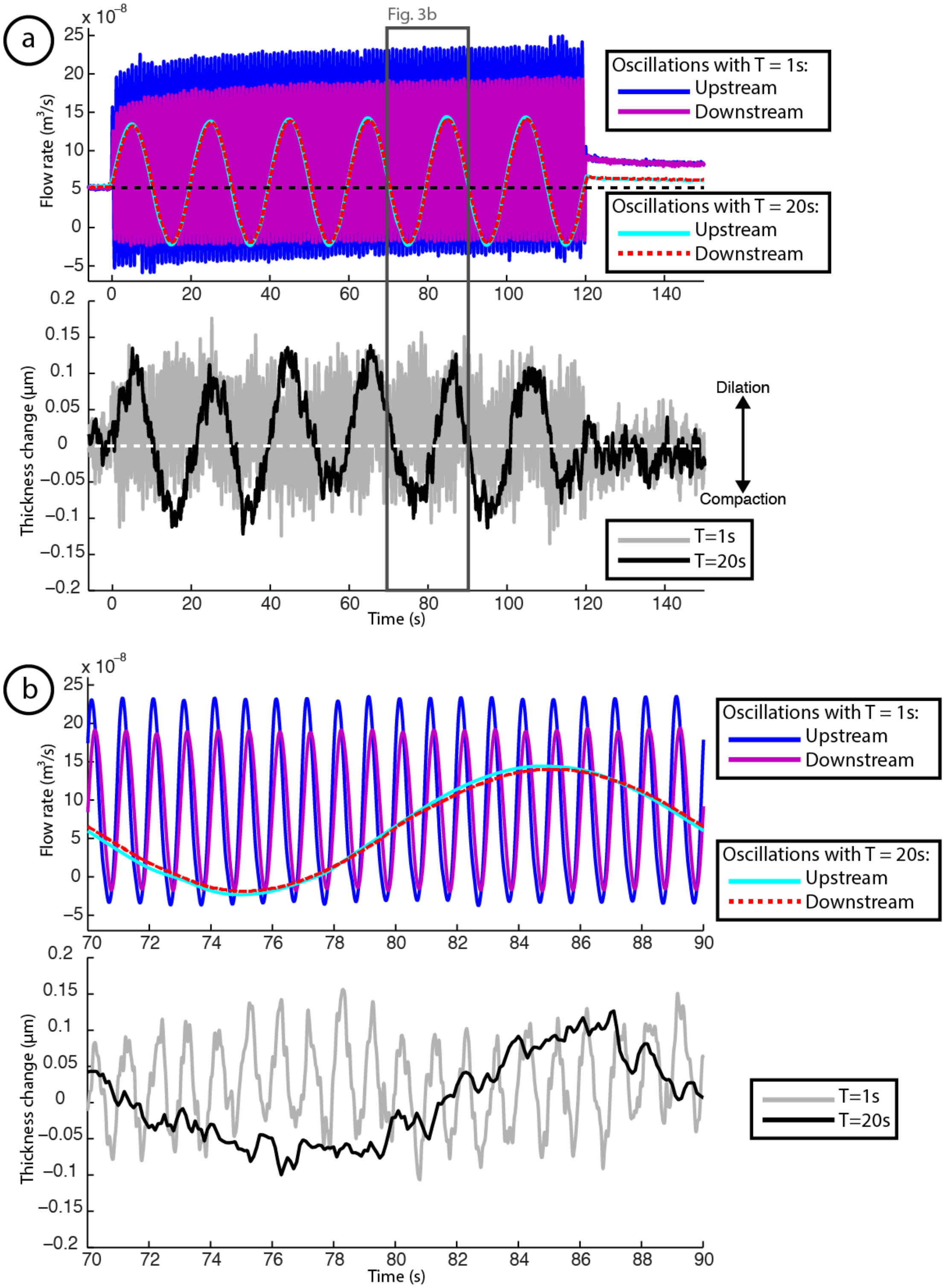

a
x 10^-8
Fig. 3b
Flow rate (m3/s)
Oscillations with T = 1s:
Upstream
Downstream
Oscillations with T = 20s:
Upstream
Downstream
Thickness change (µm)
Dilation
Compaction
T=1s
T=20s
Time (s)
b
x 10^-8
Flow rate (m3/s)
Oscillations with T = 1s:
Upstream
Downstream
Oscillations with T = 20s:
Upstream
Downstream
Thickness change (µm)
T=1s
T=20s
Time (s)

Figure 4:

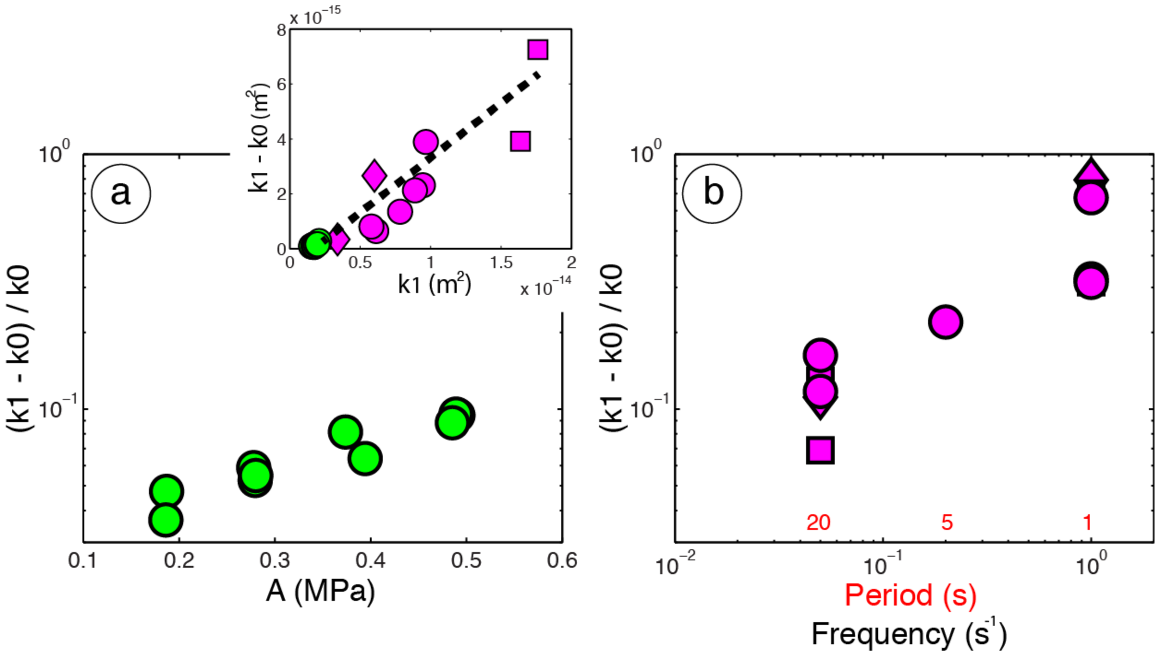

a
b
(k1 - k0) / k0
A (MPa)
0.1
0.2
0.3
0.4
0.5
0.6
k1 - k0 (m²)
k1 (m²)
x 10⁻¹⁵
x 10⁻¹⁴
Period (s)
20
5
1
Frequency (s⁻¹)

Figure 5:

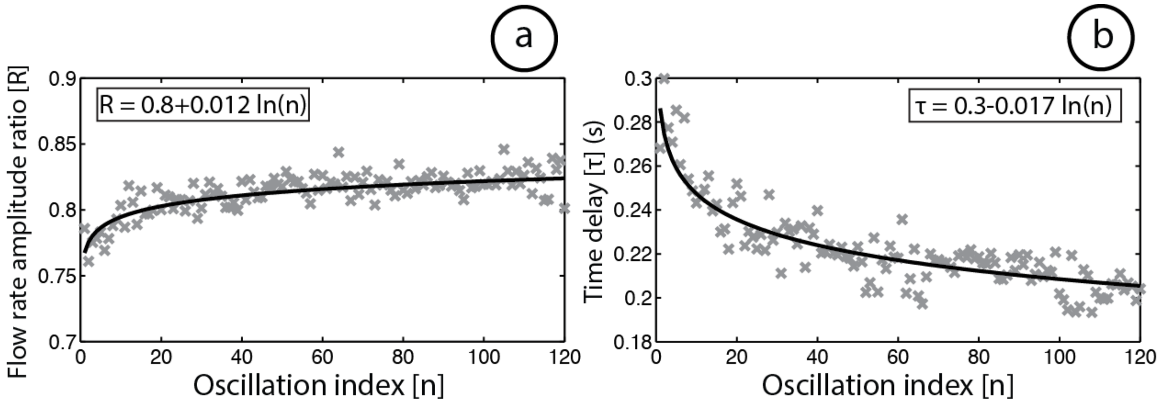

a
b
R = 0.8+0.012 ln(n)
τ = 0.3-0.017 ln(n)
Flow rate amplitude ratio [R]
Time delay [τ] (s)
Oscillation index [n]
Oscillation index [n]
0.9
0.85
0.8
0.75
0.7
0.3
0.28
0.26
0.24
0.22
0.2
0.18
0
20
40
60
80
100
120

Figure 6:

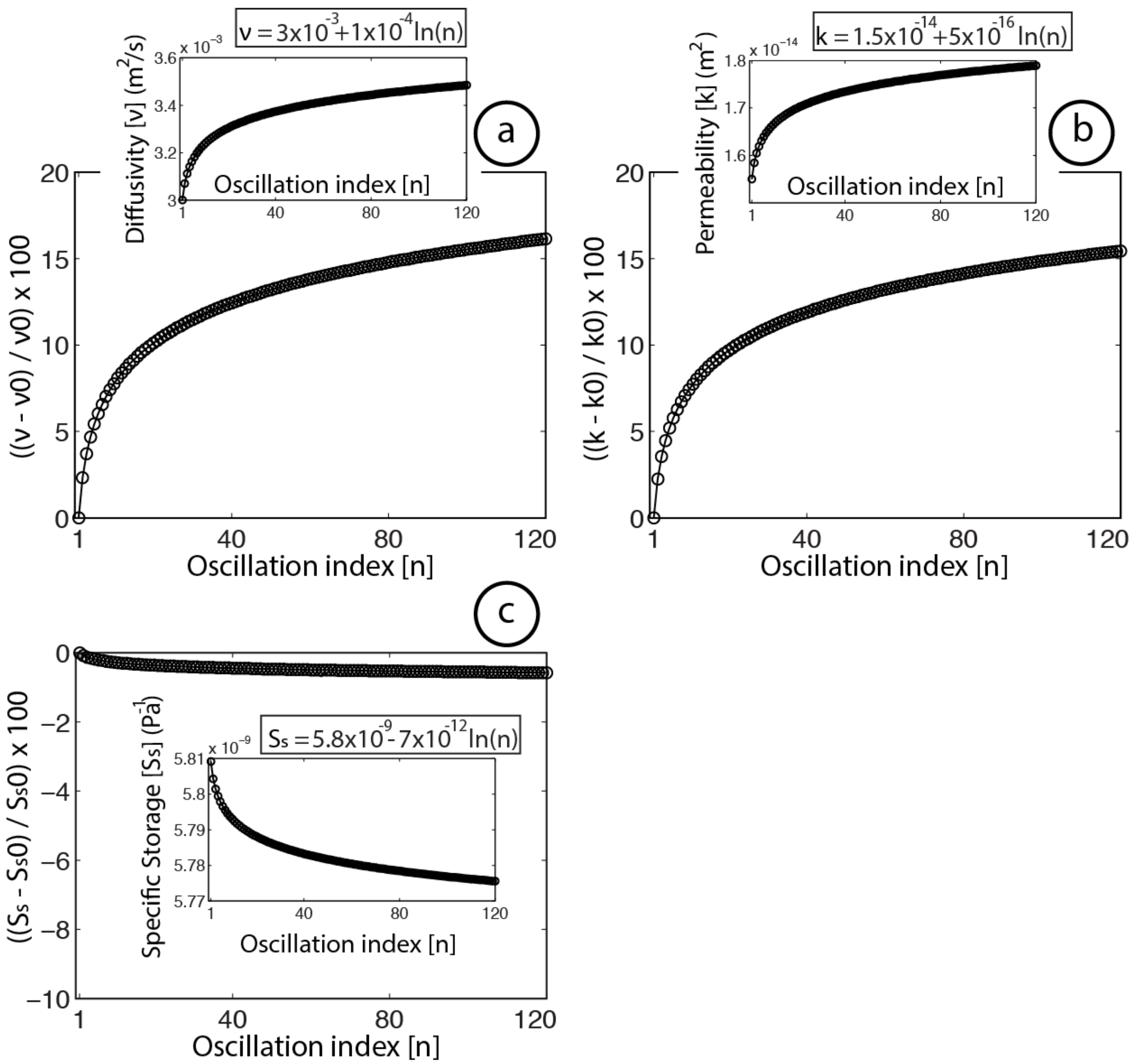

a
v = 3x10-3+1x10-4ln(n)
x 10−3
Diffusivity [v] (m2/s)
3.6
3.4
3.2
3
Oscillation index [n]
1
40
80
120
((v - v0) / v0) x 100
20
15
10
5
0
Oscillation index [n]
b
k = 1.5x10-14+5x10-16ln(n)
x 10−14
Permeability [k] (m2)
1.8
1.7
1.6
Oscillation index [n]
((k - k0) / k0) x 100
Oscillation index [n]
c
((Ss - Ss0) / Ss0) x 100
0
−2
−4
−6
−8
−10
Ss = 5.8x10-9-7x10-12ln(n)
x 10−9
Specific Storage [Ss] (Pa-1)
5.81
5.8
5.79
5.78
5.77
Oscillation index [n]
Oscillation index [n]

Figure 7:

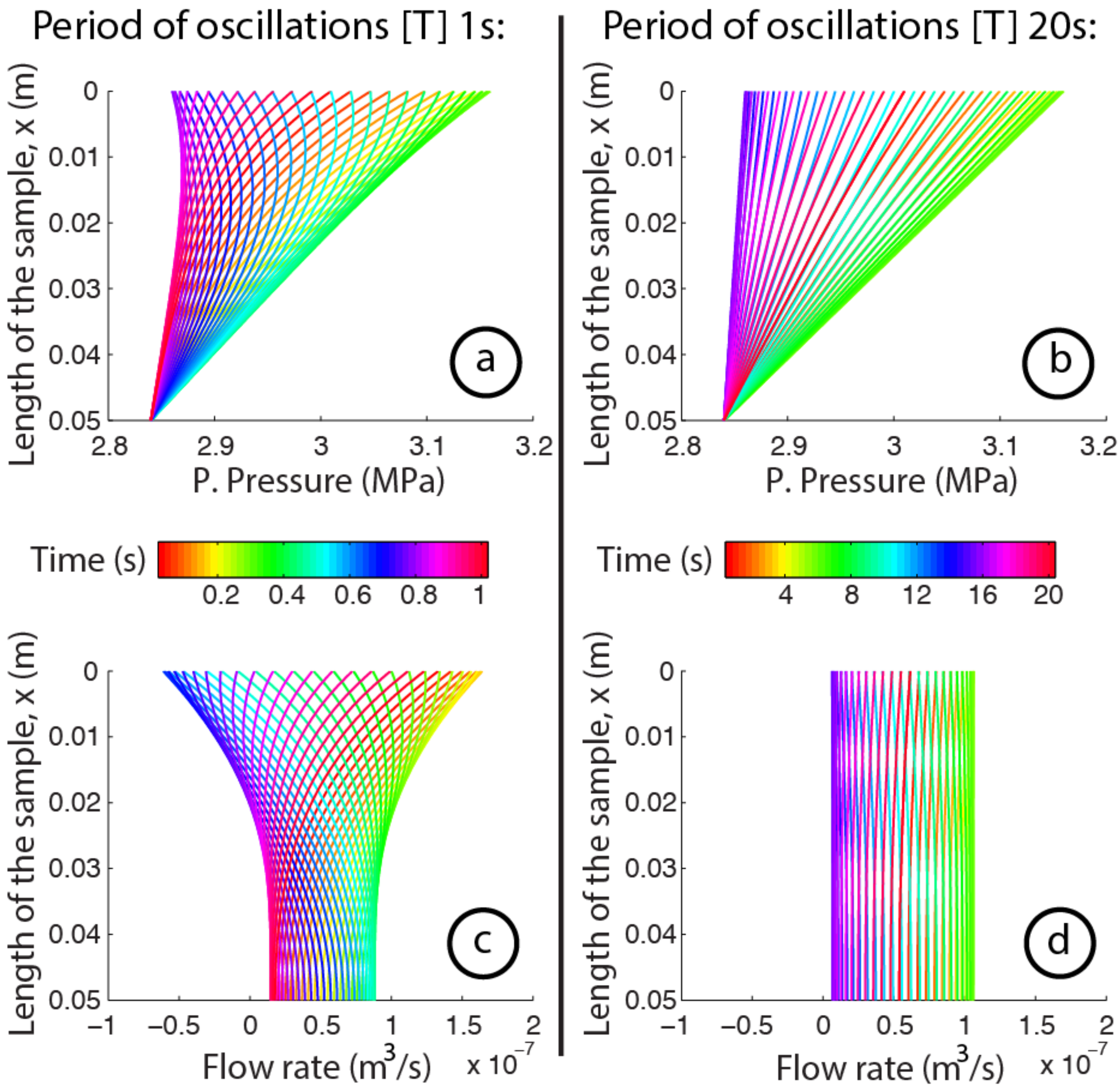

Period of oscillations [T] 1s:
Period of oscillations [T] 20s:
Length of the sample, x (m)
P. Pressure (MPa)
a
b
Time (s)
0.2 0.4 0.6 0.8 1
4 8 12 16 20
Flow rate (m3/s)
x 10−7
c
d

Figure 8:

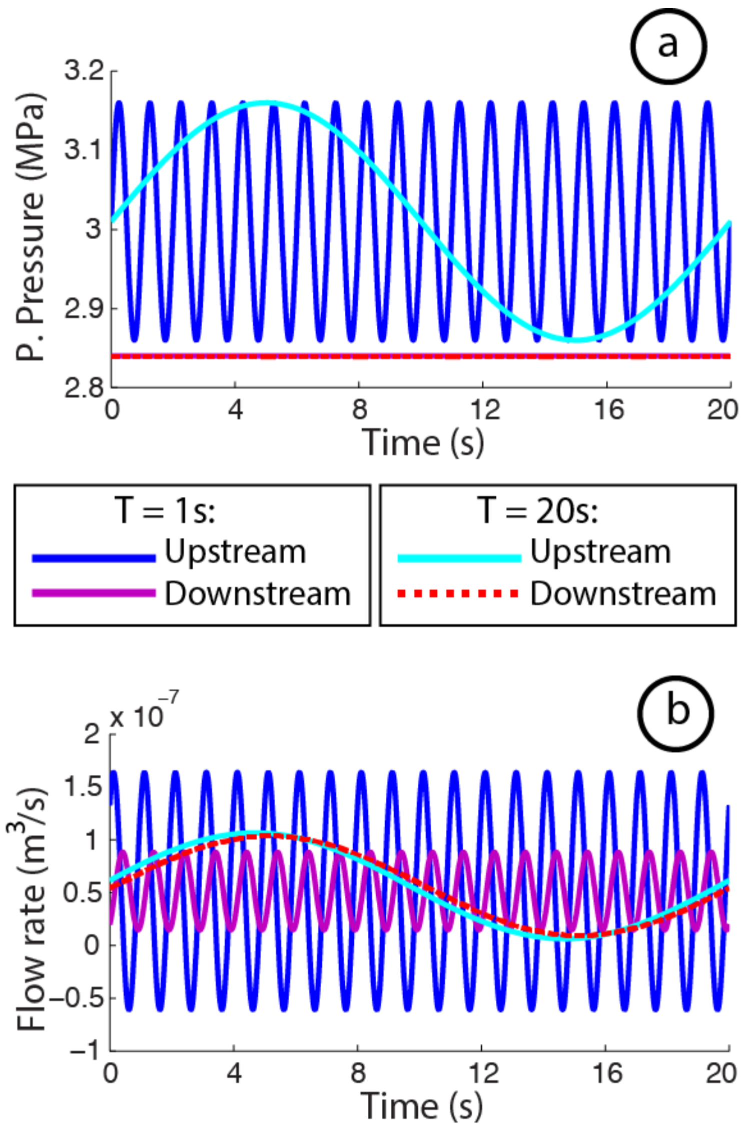
a
P. Pressure (MPa)
3.2
3.1
3
2.9
2.8
0
4
8
12
16
20
Time (s)
T = 1s:
Upstream
Downstream
T = 20s:
Upstream
Downstream
b
x 10^-7
Flow rate (m^3/s)
2
1.5
1
0.5
0
−0.5
−1
0
4
8
12
16
20
Time (s)

Figure 9:

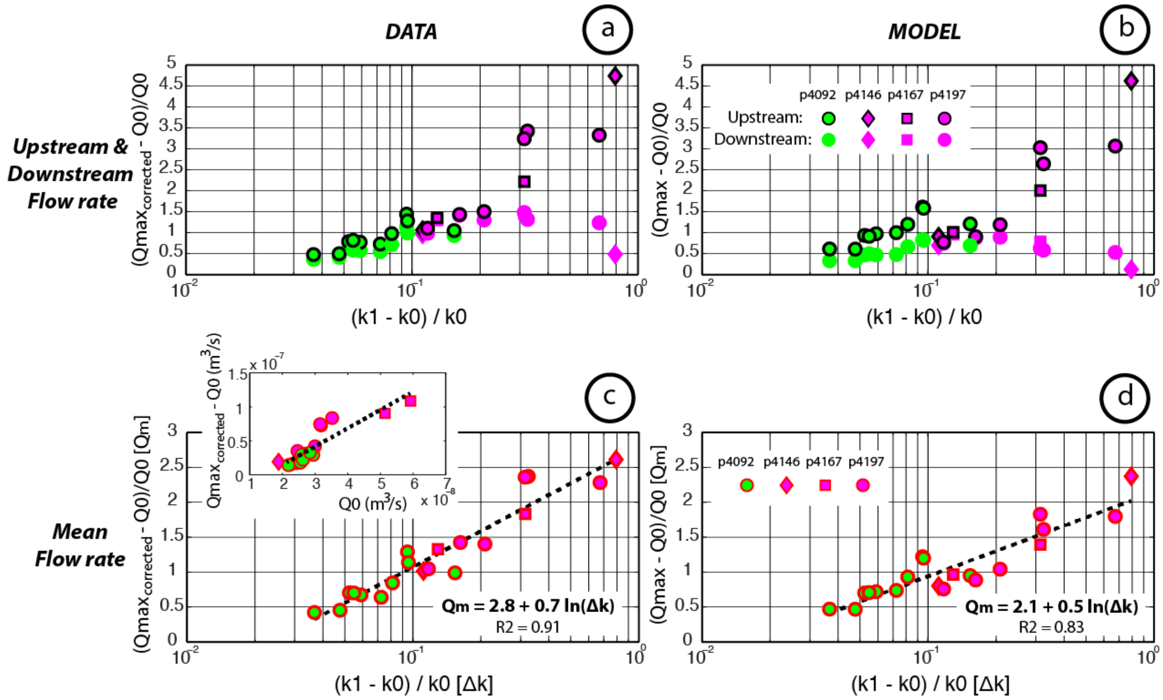
DATA
a
MODEL
b
Upstream & Downstream Flow rate
(Qmax_corrected - Q0)/Q0
(Qmax - Q0)/Q0
p4092 p4146 p4167 p4197
Upstream:
Downstream:
(k1 - k0) / k0
c
d
Mean Flow rate
(Qmax_corrected - Q0)/Q0 [Qm]
(Qmax - Q0)/Q0 [Qm]
Qmax_corrected - Q0 (m3/s)
Q0 (m3/s)
Qm = 2.8 + 0.7 ln(Δk)
R2 = 0.91
Qm = 2.1 + 0.5 ln(Δk)
R2 = 0.83
(k1 - k0) / k0 [Δk]

Figure 10:

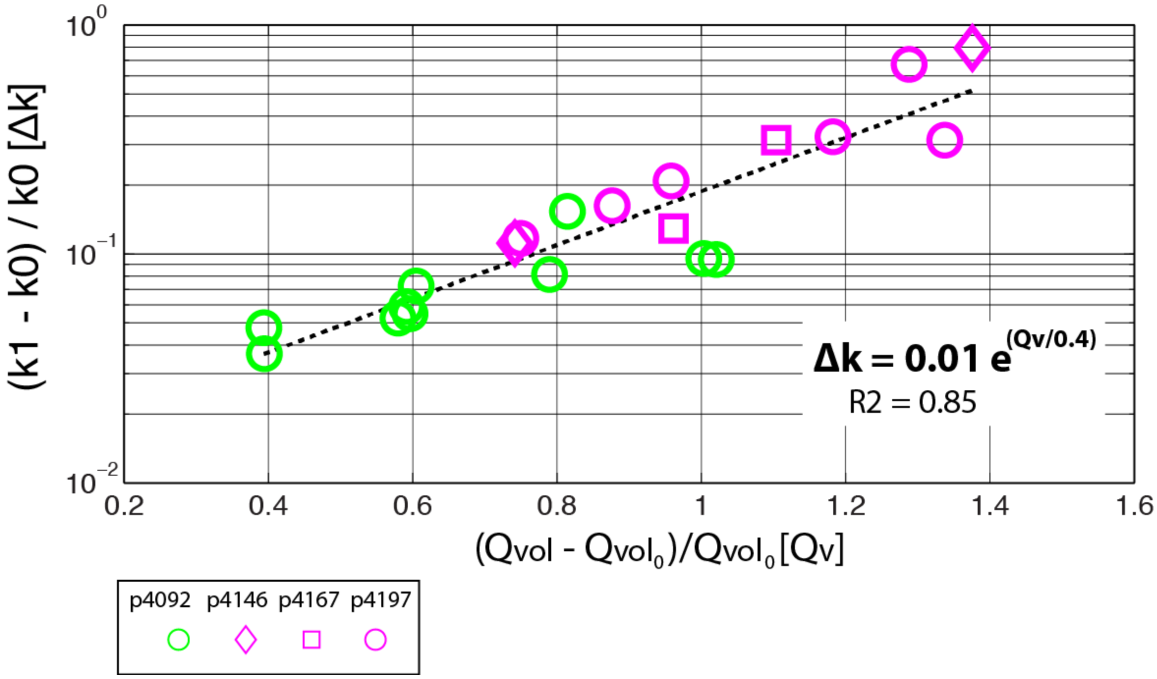

10^0
10^-1
10^-2
0.2
0.4
0.6
0.8
1
1.2
1.4
1.6
(k1 - k0) / k0 [Δk]
(Qvol - Qvol0)/Qvol0 [Qv]
Δk = 0.01 e^(Qv/0.4)
R2 = 0.85
p4092
p4146
p4167
p4197

1148 **Figure 11:**

1149

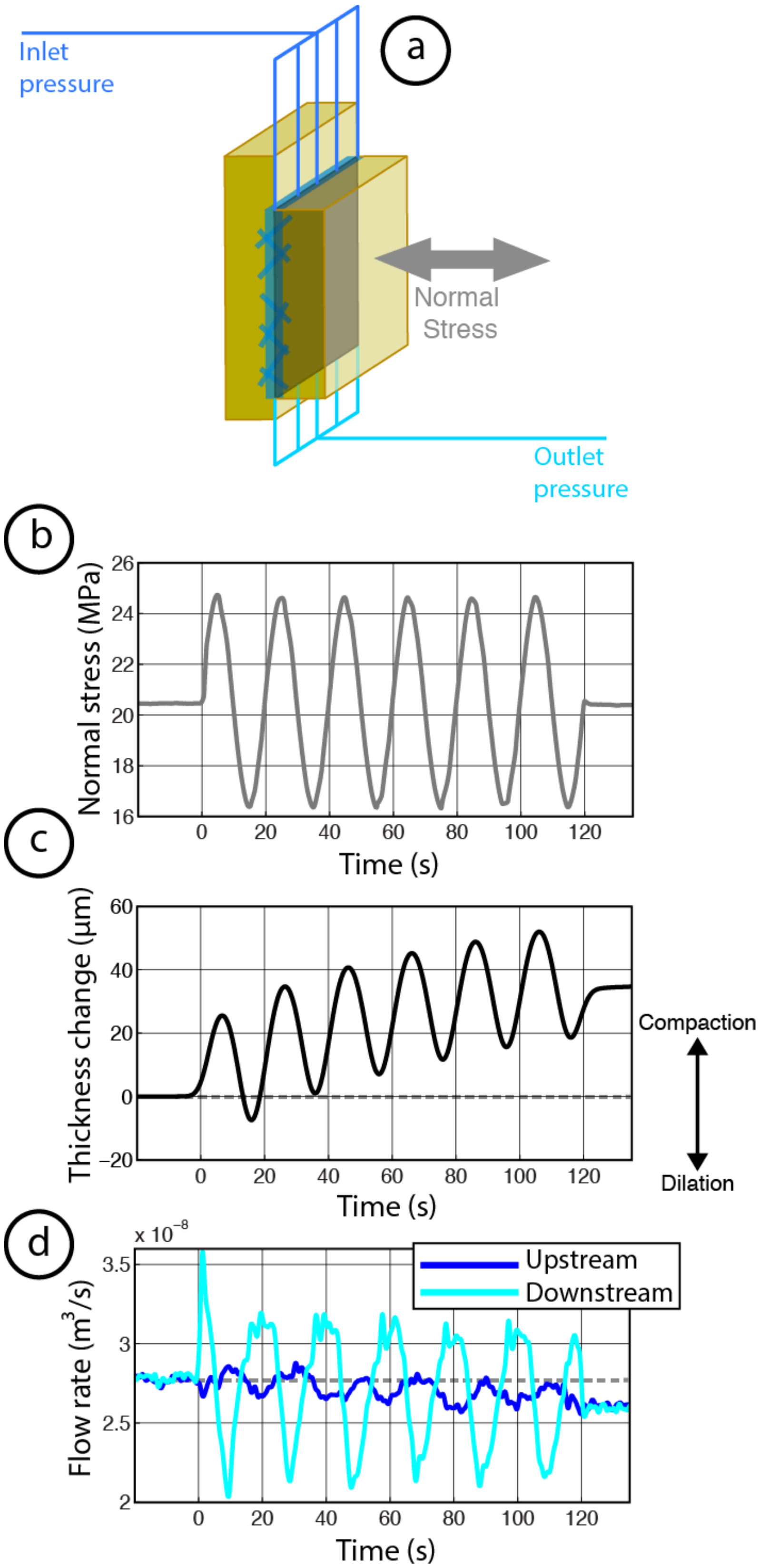

1150

Figure 12:

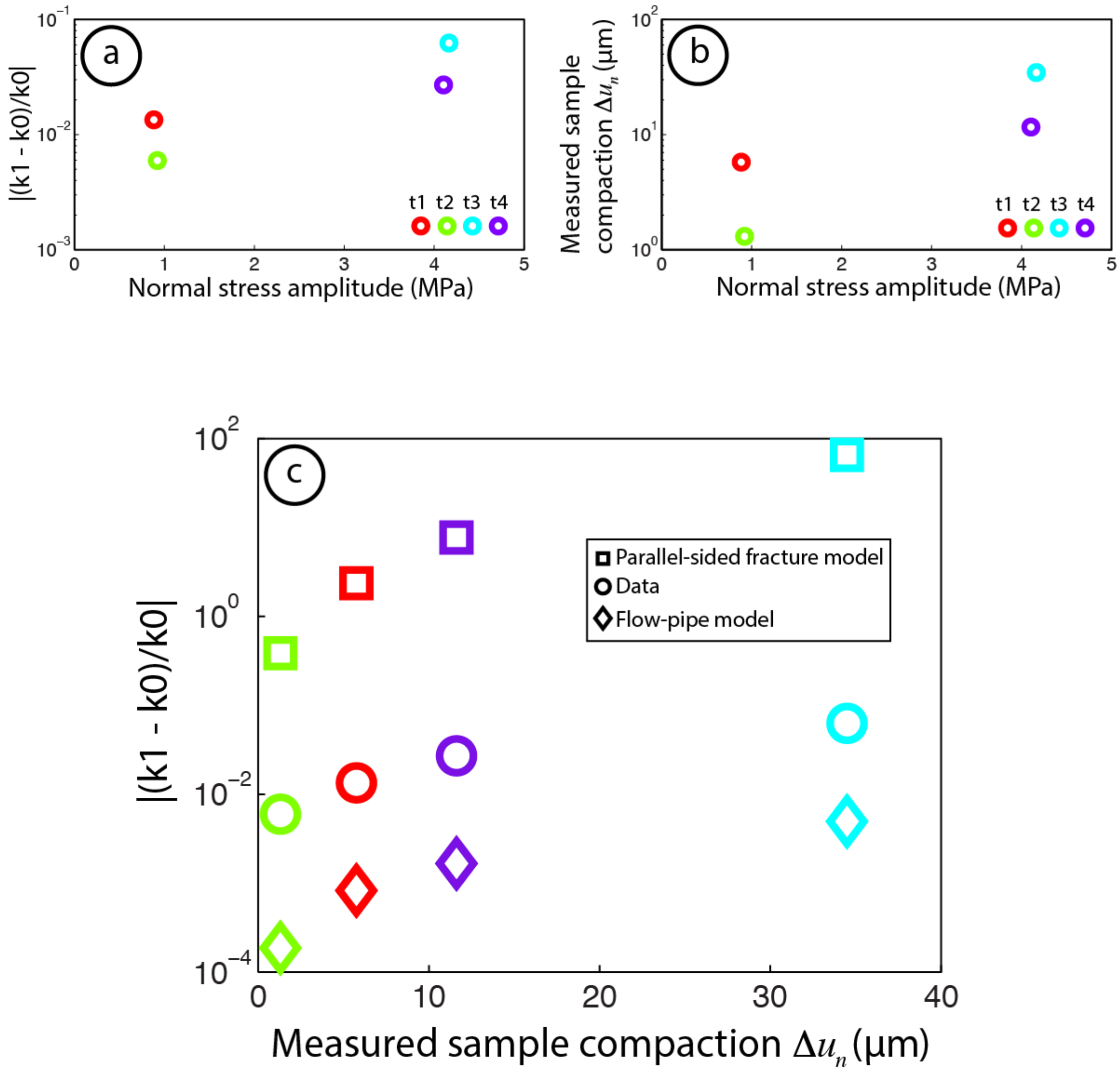

a
|(k1 - k0)/k0|
Normal stress amplitude (MPa)
t1 t2 t3 t4
b
Measured sample compaction Δu_n (μm)
Normal stress amplitude (MPa)
t1 t2 t3 t4
c
Parallel-sided fracture model
Data
Flow-pipe model
|(k1 - k0)/k0|
Measured sample compaction Δu_n (μm)